Lifetime measurements in ^{99}Nb and ^{99}Zr: Investigation of shape coexistence

A. Pfeil,[1,*] K. Nomura,[2] N. Gavrielov,[3,4] J.-M. Régis,[1] U. Köster,[5] Y. H. Kim,[6] A. Esmaylzadeh,[1] A. Harter,[1] J. Jolie,[1] L. Knafla,[1] M. Ley,[1] and V. Karayonchev[1,†]

[1]*Universität zu Köln, Institut für Kernphysik, D-50937 Köln, Germany*
[2]*Department of Physics, Hokkaido University, Sapporo 060-0810, Japan*
[3]*Center for Theoretical Physics, Yale University, New Haven, Connecticut 06520-8120, USA*
[4]*Racah Institute of Physics, The Hebrew University, Jerusalem 91904, Israel*
[5]*Institut Laue-Langevin, 71 Avenue des Martyrs, 38042 Grenoble, France*
[6]*Institute for Basic Science, 55 Expo-ro, Daejeon 34126, Korea*

(Received 23 June 2023; accepted 31 August 2023; published 19 September 2023)

The $A \approx 100$ mass region is of special interest due to a rapid shape transition, observed by going from neutron number 58 to 60, especially pronounced in the Zr isotopes, where ^{98}Zr is weakly and ^{100}Zr is strongly deformed. To further examine this intricate phenomenon, in this work lifetimes of low-lying excited states in the nuclei ^{99}Zr and ^{99}Nb were determined using fast-timing techniques and an experimental setup consisting of four $LaBr_3$(Ce) detectors. Neutron rich $A = 99$ fragments were produced in neutron induced fission and separated by the spectrometer LOHENGRIN at the Institut Laue-Langevin in Grenoble, France. Experimental values are compared to two different calculations in the framework of the interacting boson-fermion model and discussed in the context of shape coexistence.

DOI: 10.1103/PhysRevC.108.034310

I. INTRODUCTION

Nuclei in the neutron-rich $A \approx 100$ region exhibit a diverse range of shape phenomena, which can coexist within a nucleus. This region has garnered significant attention in theoretical investigations due to its complex microscopic composition. The way nucleons interact with each other plays a crucial role in determining the shell structure and leads to diverse shapes, including quantum phase transitions involving shape changes [1] as well as the coexistence of different shapes [2]. A remarkable observation is the rapid transition in ground-state deformation among the spherical ^{96}Zr, weakly deformed ^{98}Zr [3], and strongly deformed ^{100}Zr [4]. Fascinating phenomena often arise when we observe abrupt deviations from a general pattern. Generally, the properties of atomic nuclei with partially filled proton and neutron shells exhibit smooth changes as the proton number (Z) and neutron number (N) vary. However, in the case of nuclei with $Z \approx 40$ and $N \approx 60$, we observe a sudden emergence of deformation. This is particularly evident in the even-even nuclei of Sr ($Z = 38$) and Zr ($Z = 40$), where a sharp decrease in the excitation energy of the first 2^+ state, coupled with a significant increase in the $B(E2; 0_1^+ \rightarrow 2_1^+)$ values [5], is a clear indication of the dramatic onset of deformation in these nuclei. Additionally, evidence for this can be found in the nonlinear growth of charge radii observed in the chains of Rb, Sr, Y, Zr, and Nb isotopes [6]. The introduction of deformation in Zr isotopes at $N = 60$ was first explained by Sheline *et al.* as a result of the interplay between spherical and strongly deformed normal and intruder configurations, leading to shape coexistence in the transitional region [7]. The sudden emergence of deformation around $Z = 40$ and $N = 60$ is attributed to the depletion of protons from the orbitals of the $N = 3$ oscillator shell, accompanied by the occupation of $\pi g_{9/2}$ orbitals, the filling of $\nu h_{11/2}$ neutron orbitals, and the depletion of neutrons in the $\nu g_{9/2}$ orbitals [8]. The presence of $Z = 38$ ($\pi p_{3/2}$) and 40 ($\pi p_{1/2}$) proton subshell closures, combined with $N = 50$ ($\nu g_{9/2}$), 56 ($\nu d_{5/2}$), and 58 ($\nu s_{1/2}$) neutron subshell closures, and a weak residual proton-neutron interaction, create a low-energy structure in Sr and Zr isotopes that resembles that of a semimagic nucleus from $N = 50$ to 58. However, at $N = 60$, a strongly prolate deformed ground-state rotational band emerges and forms the lowest states. This change in shape occurs more gradually in the higher-Z Mo-Pd nuclei of the region across $N = 58$–60, exhibiting triaxiality [9]. At lower Z values, the $N \geqslant 60$ nuclei ^{96,98,100}Kr have been shown to possess reduced collectivity, attributed to a decreased occupation of the $\pi g_{9/2}$ orbital and the coexistence of prolate and oblate shapes [10]. The swift nature of the ground-state deformation change in this region presents a challenge for theoretical investigation. Various theoretical explanations have been proposed, including the crossing of two distinct mean-field configurations: One governed by spherical shell effects and the other a deformed intruder configuration with multiple particle-hole excitations, primarily influenced by the residual proton-neutron interaction [7]. Given that neutron-rich nuclei within this mass range

*Corresponding author: apfeil@ikp.uni-koeln.de
†Present address: Argonne National Laboratory, 9700 South Cass Ave, Argonne, IL 60439, USA.

are also involved in rapid neutron-capture processes, it becomes imperative to have accurate theoretical descriptions of their low-lying structure and transition rates. In many instances, the low-energy structure of these nuclei is so intricate that it serves as an ideal testing ground for theoretical models. Recently, numerous experimental and theoretical studies have emerged focusing on the spectroscopic properties of Zr isotopes with an even number of protons and neutrons. The majority of experimental findings have indicated the presence of shape coexistence in ^{96}Zr [11] and ^{98}Zr [12], a quantum phase transition occurring around the neutron number $N \approx 60$ [13], as well as the existence of γ-soft and triaxial shapes in ^{100,102}Zr [14]. Theoretical investigations have generally supported these experimental results [15,16]. However, there has been relatively less emphasis on studying shape-phase transitions in odd-A nuclei. Experimental evidence supporting the coexistence of spherical and deformed configurations has been observed in $^{96-98}$Sr [17,18], $^{96-104}$Y [19–21], and $^{98-100}$Zr [22–26]. A significant interaction between the occupied $\pi g_{9/2}$ and $\nu g_{7/2}$ spin-orbit partner orbitals has been proposed as a key factor in disrupting the $N = 56$, 58 and $Z = 38$, 40 spherical subshell closures, leading to collective motion [27]. Exploring the properties of shape-coexisting structures at the spherical-deformed border ($N = 59$) is of particular interest, as it may provide further insights into the underlying mechanisms driving the shape change. Currently, no comprehensive theoretical explanation exists that encompasses all shape coexisting features observed in this region, despite it being home to some of the most well-known cases in the entire nuclear landscape [2]. Crucial information regarding collectivity can be obtained from measurements of electromagnetic transition rates between different states in the bands of odd-A nuclei. The reduced $E2$ transition rate, $B(E2)$, directly correlates with quadrupole collectivity and can be derived from the measured lifetime of a stretched intraband $E2$ transition. Alternatively, measurements of intraband $B(M1)$ values, which often depend on the specific orbital, can probe the underlying single-particle structure of a band.

The structure of this work is as follows. In Sec. II, a detailed description is provided for the experiment and its setup. Section III outlines the fast-timing method utilized to determine the level lifetimes. The analysis procedures for the measured lifetimes are presented in Sec. IV. Moving on to Sec. V, the calculations and discussion are presented, comparing them to the experimental results. Lastly, a conclusion is presented in Sec. VI.

II. EXPERIMENTAL DETAILS

Isobars with $A = 99$ were produced in fission of a 119 μg/cm^2 ^{235}U oxide target covered with a 70×7 mm^2 diaphragm and a 0.25 μm thick Ni foil to reduce sputtering [28]. The cumulative fission yields of the parent nuclides ^{99}Y and ^{99}Zr, producing the nuclei of interest ^{99}Zr and ^{99}Nb after β decay, are about 1.9% and 5.9%, respectively. The fission fragments were mass separated by the LOHENGRIN spectrometer [29,30] and implanted into an aluminum foil inside the target chamber. The experimental setup consisted of four cylindrical 1.5 in. × 1.5 in. cerium doped lanthanum bromide [$LaBr_3$(Ce)] detectors, surrounding the target chamber and installed as close as possible to all sides of the target chamber to maximize the efficiency as previously used in other experiments [31]. This results in a distance of 2.2 cm between detectors and the center of the implantation zone (rectangular spot about 1×3 cm^2). No shielding was used to minimize the distance between implantation zone and detectors and to avoid contaminating x rays from the shielding material that could lead to false coincidences in the region below 100 keV, where some of the γ rays in this experiment are located. In this compact geometry, the efficiency for each $LaBr_3$(Ce) detector is about 3.7% at 122 keV [32]. In addition to the four $LaBr_3$(Ce) scintillators, a high purity germanium (HPGe) clover with four individual crystals was mounted directly above the target chamber for high resolution monitoring of the emitted γ rays. The combined efficiency of the clover is around 3.8% at 122 keV [32]. The experimental setup used for this work is comparable to the setups described in [31], but with improved placement of the clover detector to further increase efficiency.

Due to accumulated activity of implanted $A = 99$ fission fragments and their following β decays, different $A = 99$ isobars are accessible. The relative β decay activity of a given isobar is roughly proportional to its cumulative fission yield.

To analyze the nuclei ^{99}Zr and ^{99}Nb, the selected mass was $A = 99$ with a charge state of $q = 21$ and an energy of $E = 92$ MeV. This setting leads to contamination from $A = 85$, 94, and 104, since all have similar A/q ratios. While this setting produced several contaminants it was used due to its significantly higher yield, compared to other potential more selective settings. For this reason, not only the β decay chains of ^{99}X but also of ^{85}X, ^{94}X, and ^{104}X are visible as contaminants in the measured spectra. All data recorded for this experiment can be found in Ref. [33] .

III. FAST-TIMING METHOD

In order to determine lifetimes of excited states in ^{99}Nb and ^{99}Zr the γ-γ fast-timing method using $LaBr_3$(Ce) detectors was performed. The basic idea of this method is the measurement of time differences between two electronic signals, generated by the detection of selected γ rays populating and de-exciting the state of interest. The lifetime is then obtained by correcting the measured time difference by the systematic influence of the measurement device [34,35]. To measure the time difference between two coincident γ rays it is necessary to generate electronic signals that hold time and energy information. A common setup basically consists of at least two detectors, two constant fraction discriminators (CFD), a time-to-amplitude converter (TAC) connected to the data-acquisition system (DAQ). In the DAQ the obtained information about E_{start}, E_{stop}, and Δt are written in list-mode files which are used in the offline analysis to create $LaBr_3$(Ce)-$LaBr_3$(Ce) events. From these events, asymmetric E_{start}-E_{stop}-Δt matrices are constructed for generation of time-difference distribution using gates set on the E_{start} and E_{stop} axes [34,36].

Using four $LaBr_3$(Ce) detectors results in six individual detector-detector combinations in total. In order to improve

the time resolution, a time alignment of these combinations must be performed. Furthermore, the exclusion of nearest neighbor γ-γ coincidences can be used to minimize the effects of inter detector scattering, if present. This reduces the statistics, but also the background and so-called "ghost peaks" can also be prevented [37]. The final γ-γ time difference distributions consist of two identical mirror-symmetric distributions (delayed/antidelayed). Assuming no background contributions, the delayed time distribution $D(t)$ can be written as a convolution of the prompt-response function (PRF) $P(t' - t_0)$ and an exponential decay [36]:

$$D(t) = n\lambda \int_{-\infty}^{t} P(t' - t_0) e^{-\lambda(t-t')} dt' + n_r, \quad \lambda = 1/\tau. \quad (1)$$

Here, n describes the total counts in the time distribution and n_r are constant random counts. The centroid C^D of a delayed time distribution is defined as the first moment of the statistical time distribution $D(t)$ [34]:

$$C^D = \langle t \rangle = \frac{\int_{-\infty}^{\infty} t \cdot D(t) dt}{\int_{-\infty}^{\infty} D(t) dt} \quad (2)$$

with a uncertainty of $\delta C^D \approx \delta t = \frac{\sigma}{\sqrt{n}}$. For more details see Ref. [34]. According to Ref. [40], the centroid of a time distribution $D(t)$ is shifting by the mean lifetime from the centroid t_0 of the PRF. Using the generalized centroid difference (GCD) method, an extended version of the mirror symmetric centroid difference method for setups with more than two detectors, lifetimes of states of interest can be determined from the centroid difference between delayed and antidelayed time distributions and the combined time response of the used setup [36,41]:

$$\Delta C(E_{\text{feeder}}, E_{\text{decay}}) = \text{PRD}(E_{\text{feeder}}, E_{\text{decay}}) + 2\tau, \quad (3)$$

where ΔC is the centroid difference of delayed and antidelayed time distributions, whereas the prompt response difference (PRD) describes the combined γ-γ energy-dependent time response of the used setup [41]. Therefore, the PRD has to be calibrated precisely using full energy peaks (FEP) of well-known calibration sources. Here, the γ rays from the decay of the ^{152}Eu, ^{185}Os, and ^{187}W sources were used to produce data points in a wide energy range. For a detailed description of the calibration procedure see Ref. [34]. To obtain the final PRD curve, shown in Fig. 1, the following function was fitted to the data points [37]:

$$\text{PRD}(E_\gamma) = \frac{a}{\sqrt{E_\gamma + b}} + cE_\gamma^2 + dE_\gamma + e. \quad (4)$$

Values for the PRD can be easily derived from Fig. 1, where $\text{PRD}(E_{\text{feeder}}, E_{\text{decay}}) = \text{PRD}(E_{\text{feeder}}) - \text{PRD}(E_{\text{decay}})$.

It should be noted that Eqs. (1) and (3) are only valid for the assumption of no time-correlated background affecting the measured centroid difference. Since this is rarely the case, the experimentally measured centroid difference has to be corrected for possible background contributions. It is not possible to directly measure the timing behavior of the background beneath the full energy peaks itself. Therefore, an analytical background correction can be used to interpolate the background at the energy of interest by using several gates

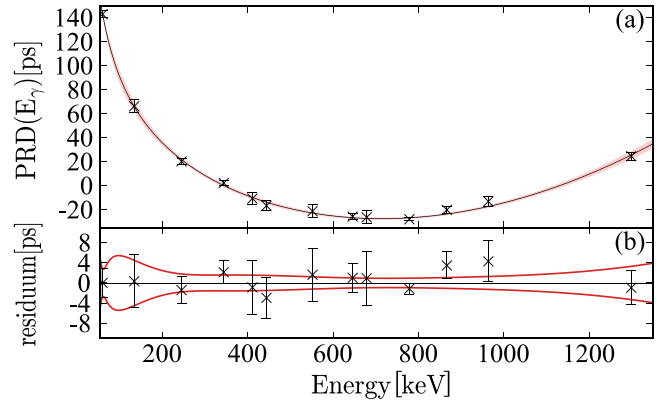

FIG. 1. (a) PRD curve determined from ^{152}Eu, ^{185}Os, and ^{187}W sources and using Eq. (4) as fit function. Known lifetimes for the data points are taken from [38,39]. (b) Fit residuals of the PRD curve. The 1σ uncertainty band is plotted in red.

on the background around the FEP. A reliable way to correct the timing influence on the experimental determined centroid is to derive a correction factor $\tilde{t}_{\text{cor}}$ as outlined in Refs. [13,42]:

$$\Delta C = \Delta C_{\text{exp}} + \tilde{t}_{\text{cor}}. \quad (5)$$

Since both decaying and feeding transitions are affected by the time correlated background, the influence on both peaks has to be corrected [32]:

$$\tilde{t}_{\text{cor}} = \frac{P/B(E_f) \cdot t_{\text{cor}}(E_i) + P/B(E_i) \cdot t_{\text{cor}}(E_f)}{P/B(E_i) + P/B(E_f)} \quad (6)$$

with

$$t_{\text{cor}}(E_i) = \frac{\Delta C_{\text{exp}} - \Delta C_{\text{Compton}}}{P/B(E_i)}. \quad (7)$$

Equation (6) corresponds to a weighted average of the corresponding correction terms for the feeding and decaying transitions weighted by its peak-to-background ratio $[P/B(E_i)]$, whereas $\Delta C_{\text{Compton}}$ describes the interpolated centroid difference of the time-correlated background underneath the FEPs. All uncertainties are calculated via the Gaussian error propagation.

IV. ANALYSIS

In this work the lifetimes of the $(7/2_1^+)$, $(5/2_1)^+$, $3/2_1^-$, and $(1/2^+, 3/2^+)$ states in ^{99}Nb and the lifetimes of the $(3/2_1^+)$, $(3/2_2^+)$, and $(3/2_3^+)$ states in ^{99}Zr were measured. Figure 2 shows the full projection spectra of the $LaBr_3$(Ce) and HPGe twofold coincidences in the relevant energy range. Thus, only these γ rays are displayed when either two $LaBr_3$(Ce) detectors or one $LaBr_3$(Ce) and one HPGe are triggered within the selected time window of 1 µs. The better energy resolution of the HPGe crystals is used to check the $LaBr_3$(Ce) spectrum for contaminants. All relevant transitions used for the lifetime measurement in this work are marked in Fig. 2. The peaks that are not marked mostly stem from the $A = 85$, 94, and 104 masses which have similar A/q ratio. Partial level schemes after β decay for both nuclei, ^{99}Nb and ^{99}Zr, respectively, including all used transitions are shown in Fig. 3. All but one

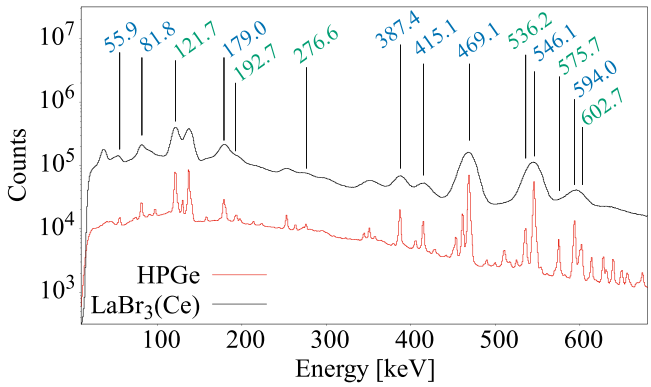

FIG. 2. Full projections of $LaBr_3(Ce)$-$LaBr_3(Ce)$ (black) and $LaBr_3(Ce)$-HPGe (red) twofold coincidences without any energy conditions applied and within a 1 µs coincidence window. Relevant transitions [38] for the determination of lifetimes in the ^{99}Zr and ^{99}Nb nuclei are marked in green and blue, respectively. The peaks that are not marked mostly stem from the $A = 85$, 94, and 104 masses which have a similar A/q ratio.

lifetime were analyzed in twofold [$LaBr_3(Ce)$-$LaBr_3(Ce)$] coincidences. Only for the $(3/2_3^+)$ state in ^{99}Zr the statistics were sufficient to allow the use of threefold [HPGe-$LaBr_3(Ce)$-$LaBr_3(Ce)$] coincidences with a clover gate on the 122 keV line for precise selection of the cascade of interest. All lifetimes were analyzed using the GCD method and lifetimes longer than 200 ps are additionally analyzed using the convolution and/or slope method [50]. The lifetime measurement procedure is exemplary shown for the $(5/2_1)^+$ state in ^{99}Nb and all other lifetimes are measured accordingly. The results of all lifetime measurements are combined in Table I.

A. $(5/2_1)^+$ state in ^{99}Nb

The first $(5/2)^+$ state in ^{99}Nb is located at an excitation energy of 469.1 keV. This lifetime is determined using the $(3/2_3)^+ \rightarrow (5/2_1)^+ \rightarrow 9/2^+_{g.s.}$ (546.1–469.1 keV) cascade. The gated energy spectra are shown in Figs. 4(a) and (b). The corresponding peak-to-background ratios are around 31 for the peak at 546.1 keV and 35 for the peak at 469.1 keV. It can be clearly seen that both peaks of the $LaBr_3(Ce)$ spectrum are not contaminated with other γ rays (peaks). The background correction including interpolation of the time-correlated background at the energy of both FEPs are shown in Figs. 4(c) and (d). For the determination of the lifetime of the $(5/2_1)^+$ state, three different methods are used, i.e., the slope, the convolution, and the centroid difference method. The different methods and the corresponding time distributions are shown in Figs. 4(e), (f), and (g). With $\tau_{Slope} = 236(16)$ ps, $\tau_{Convolution} = 232(6)$ ps, and $\tau_{GCD} = 228(1)$ ps, all three values are consistent within its 1σ uncertainties. Since no background corrections are available for the slope and convo-

TABLE I. Final results of all measured lifetimes of ^{99}Nb and ^{99}Zr, where P/B describes the peak-to-background ratios of the used full energy peaks. All lifetimes were determined using the GCD method, except the $(3/2_1^+)$ state of ^{99}Zr which was determined using the slope method. The $(5/2_1)^+$ state of ^{99}Nb and the $(3/2_2^+)$ state of ^{99}Zr were additionally determined using the slope and convolution method. Final adopted values used for further calculations are presented in bold.

Nucleus	State	Transition	Gate [keV]	P/B	τ_{exp} [ps]	τ_{lit} [ps]
^{99}Nb	$(7/2_1^+)$	$(5/2_1)^+ \rightarrow (7/2_1^+)$	81.8	7.0(3)	**GCD: 22(3)**	25(6)[43]
		$(7/2_1^+) \rightarrow 9/2^+_{g.s.}$	387.4	7.0(3)		17(7)[44]
	$(5/2_1)^+$	$(3/2_3)^+ \rightarrow (5/2_1)^+$	546.1	31.4(4)	**GCD: 228(1)**	250(6)[43], 253(7)[44]
		$(5/2_1)^+ \rightarrow 9/2^+_{g.s.}$	469.1	34.6(4)	Slope: 236(16)	260(130)[45], 303(87)[46]
					Convolution: 232(6)	
	$3/2_1^-$	$(1/2^+, 3/2^+) \rightarrow 3/2_1^-$	415.1	7.6(3)	**GCD: 113(2)**	81(14)[43], 74(19)[44]
		$3/2_1^- \rightarrow 1/2_1^-$	179.0	15.5(4)		375(245)[45], 87(289)[47]
	$(1/2^+, 3/2^+)$	$(3/2_3)^+ \rightarrow (1/2^+, 3/2^+)$	55.9	2.5(2)	**GCD: 7(3)**	<10[43]
		$(1/2^+, 3/2^+) \rightarrow 1/2_1^-$	594.0	6.3(3)		43(19)[45]
^{99}Zr	$(3/2_1^+)$	$(3/2^+, 5/2^+) \rightarrow (3/2_1^+)$	602.7	4.9(3)	**Slope: 1561(34)**	1298(144)[47], 1544(43)[48]
		$(3/2_1^+) \rightarrow (1/2^+_{g.s.})$	121.7	3.5(1)		1550(90)[49]
	$(3/2_2^+)$	$(5/2_2^+) \rightarrow (3/2_2^+)$	276.6	0.8(1)	**GCD: 437(18)**	476(29)[48]
		$(3/2_2^+) \rightarrow (1/2^+_{g.s.})$	575.7	0.9(1)	Slope: 388(36)	
					Convolution: 375(28)	
	$(3/2_3^+)$	$(5/2_1^+) \rightarrow (3/2_3^+)$	192.7	2.8(3)	**GCD: 26(5)**	35(13)[49]
		$(3/2_3^+) \rightarrow (3/2_1^+)$	536.2	5.6(4)		

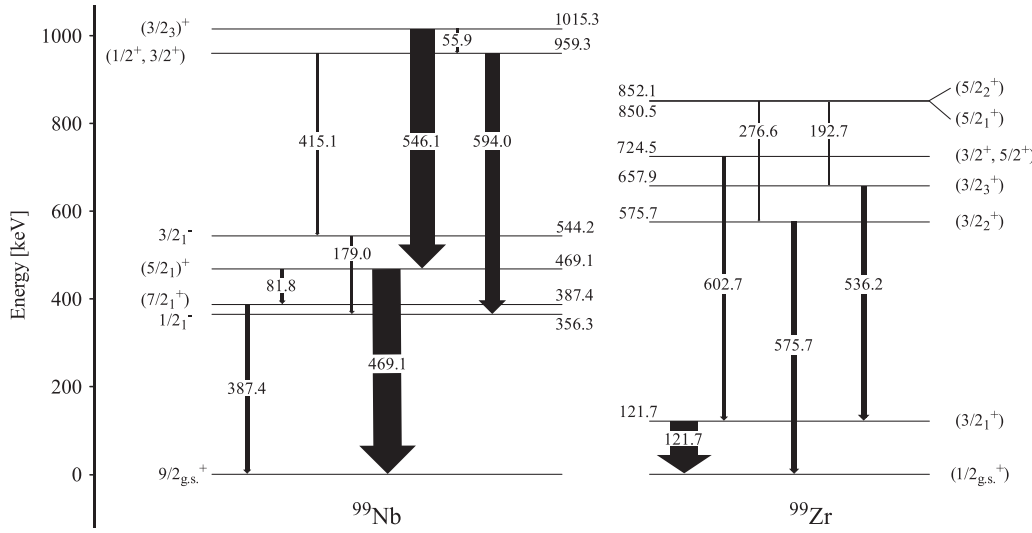

FIG. 3. Partial energy level scheme after β decay for both nuclei, ^{99}Nb and ^{99}Zr, respectively [38]. The scheme only contains transitions used to determine the lifetimes of this work.

lution method, the final adopted value for further calculations is the determined lifetime of the centroid difference method: $\tau_{(5/2_1)^+} = 228(1)$ ps.

B. Experimental results

In the latest ENSDF evaluation different lifetimes are compiled for the $(5/2_1)^+$ state: (250(6) ps [43], 253(7) ps [44], 260(130) ps [45], and 303(87) ps [46]). Here, our result is overlapping with the 3σ uncertainty of the first two literature values, whereby the others have very large uncertainties. In Ref. [43] β-γ coincidences were measured using plastic scintillators for the β detection and BaF_2 detectors for the γ particles. BaF_2 detectors have similar timing properties compared to $LaBr_3$(Ce) detectors, but their energy resolution is worse. Therefore, contaminations of nearby FEPs could occur, which could affect the transition of interest and thus the determined lifetime. In Refs. [45,46] β-γ coincidences were also measured, but instead of BaF_2 detectors, Ge detectors were used for the γ ray detection. Timing properties of Ge detectors are worse compared to $LaBr_3$(Ce), leading to the assumption that the improvement of the lifetime measurement technique using $LaBr_3$(Ce) detectors leads to more reliable results.

For the $(7/2_1^+)$ state in ^{99}Nb and the $(3/2_1^+)$ and $(3/2_3^+)$ states in ^{99}Zr the experimentally determined lifetimes fit within the 1σ uncertainties of lifetimes from the latest ENSDF evaluation but with significantly decreased uncertainties.

For the $(3/2_2^+)$ state in ^{99}Zr, the final result of the GCD method also fits within the 1σ uncertainties of previously measured lifetimes, but the results of the slope and convolution methods differs greatly. More than half of all counts in the time distributions correspond to time-correlated Compton background ($P/B < 1$). Since time-correlated background has a short lifetime in this case, these counts are mainly located around the convoluted PRF of the (delayed) time distribution and are absent or rare at the tail/slope. This effect leads to steeper distributions and hence shorter lifetimes for the slope and convolution methods than states with very good peak-to-background ratios [e.g., $(5/2_1)^+$ state in ^{99}Nb]. This also explains the difference in lifetimes between the slope and convolution method, since the convolution method accounts for even more counts of the fast background component, resulting in an even shorter lifetime.

For the $(1/2^+, 3/2^+)$ state in ^{99}Nb two different lifetimes can be found on ENSDF: (<10 ps [43] and 43(19) ps [45]). The measurement in Ref. [45] was performed using Ge detectors for the γ ray detection. Since BaF_2 detectors used in Ref. [43] have better timing properties, the measured upper limit of this lifetime is more reliable and can be confirmed by the determined lifetime of this work: $\tau = 7(3)$ ps.

Further discrepancies are between lifetimes found in literature and the lifetime determined in this work for the $3/2_1^-$ state in ^{99}Nb. While lifetimes found in Refs. [43,44] are overlapping with the 2σ uncertainties, those found in Refs. [45,47] have very large uncertainties. The setup of Ref. [47] consisted of Ge detectors for the detection of the feeding γ and BaF_2 detectors for the detection of the decaying γ. As explained before, Ge detectors have worse timing resolution, while BaF_2 detectors have worse energy resolution compared to $LaBr_3$(Ce) detectors, which might be the reason for deviating results.

V. CALCULATIONS AND DISCUSSION

A. Theoretical framework

Developing new theoretical models is essential in order to obtain knowledge of the behavior of nucleons in this mass region, especially for odd-A nuclei where the description of low lying levels is more complex than even-even nuclei due to additional interactions between the boson core and the single fermion. Therefore, probing new models and comparing them to experimentally determined data allows more insight into the underlying structure and collective motion of nucleons.

In this work we use calculations in the framework of the interacting boson-fermion model (IBFM) [51], introduced by

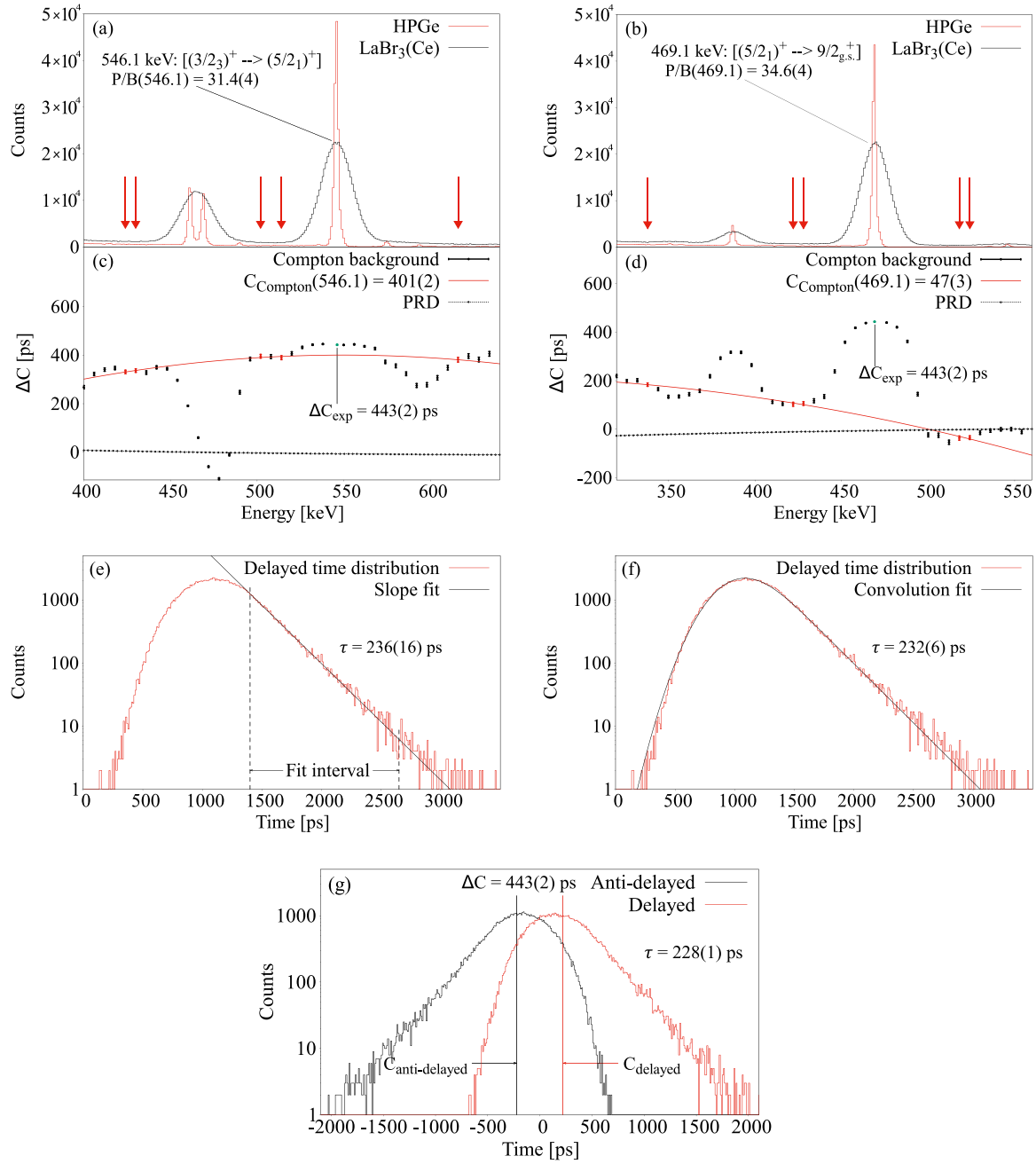

FIG. 4. (a) Energy spectra from HPGe and $LaBr_3(Ce)$ detectors showing the 546.1 keV feeding transition of the $(5/2_1)^+$ state in ^{99}Nb, gated on the $(5/2_1)^+ \rightarrow 9/2^+_{g.s.}$ (469.1 keV) transition in a spectrum measured by another $LaBr_3(Ce)$ detector. (b) Energy spectra from HPGe and $LaBr_3(Ce)$ detectors showing the 469.1 keV decaying transition of the $(5/2_1)^+$ state in ^{99}Nb, gated on the $(3/2_3)^+ \rightarrow (5/2_1)^+$ (546.1 keV) transition in a spectrum measured by another $LaBr_3(Ce)$ detector. (c) Interpolated Compton background time response of the feeding transition. Data points in red [also labeled in the corresponding energy spectrum (a)] are used for the fitted curve. (d) Interpolated Compton background time response of the decaying transition. Data points in red [also labeled in the corresponding energy spectrum (b)] are used for the fitted curve. (e) Slope and convolution (f) method for the delayed time distribution of the $(5/2_1)^+$ state using gates on the $(3/2_3)^+ \rightarrow (5/2_1)^+$ feeding transition at 546.1 keV and the $(5/2_1)^+ \rightarrow 9/2^+_{g.s.}$ decaying transition at 469.1 keV. The antidelayed distribution was mirrored and summed up to increase statistics. The dashed lines in (e) represent the fit interval for the slope method. (g) Delayed and antidelayed time distribution for the $(5/2_1)^+$ state using $LaBr_3(Ce)$ gates on the $(3/2_3)^+ \rightarrow (5/2_1)^+$ feeding transition at 546.1 keV and on the $(5/2_1)^+ \rightarrow 9/2^+_{g.s.}$ decaying transition at 469.1 keV.

Iachello and Scholten in Ref. [52], and compare them to energies and $E2$ and $M1$ transition rates of ^{99}Zr and ^{99}Nb. In the IBFM, low-lying states of odd-A nuclei are described by coupling a fermion to an even-even core nucleus, the latter represented by the monopole (s) and quadrupole (d) bosons associated with valence nucleon pairs. This leads to a Hamiltonian consisting of the boson and single fermion Hamiltonians, and the boson-fermion interactions [51]. For ^{99}Zr, we use the self-consistent mean-field (SCMF)-IBFM developed by Nomura *et al.* [53] which has already been compared to odd-A Zr isotopes in Ref. [15]. In the current work we present calculated energy levels and reduced transition probabilities not shown in [15]. For ^{99}Nb, we use the IBFM-configuration mixing (CM) developed by Gavrielov *et al.* [54], which was employed for $^{93-103}$Nb [54,55]. In the current work we present results for the negative-parity states not shown in [55].

Since both models consider odd-A nuclei in the same mass range it should be noted that several different approaches are used which are outlined in the following. In contrast to the SCMF-IBFM, the IBFM-CM model does not distinguish between protons and neutrons. In addition, the IBFM-CM includes shape coexistence which is not included in the SCMF-IBFM. Furthermore, the results of the IBFM-CM are obtained by fitting experimental data to the model, while the SCMF-IBFM determine its results through direct calculations of the theoretical model.

1. IBFM-CM

The IBFM-CM [54] is an extension of the IBFM that includes core excitations, which results in a boson-fermion model with configuration mixing, with a Hamiltonian

$$\hat{H} = \hat{H}_{\rm b} + \hat{H}_{\rm f} + \hat{V}_{\rm bf}. \tag{8}$$

In Eq. (8), $\hat{H}_{\rm b}$ is the boson core Hamiltonian, $\hat{H}_{\rm f}$ is fermion single-particle Hamiltonian, and $\hat{V}_{\rm bf}$ is the boson-fermion interaction. For multiple shell model configurations, different shell model spaces of 0p-0h, 2p-2h, 4p-4h,... particle-hole excitations are associated with the corresponding boson spaces of $N_{\rm b}, N_{\rm b}+2, N_{\rm b}+4, \ldots$ bosons, respectively, that are mixed. The boson Hamiltonian ($\hat{H}_{\rm b}$) is that of the configuration mixing model (IBM-CM) [56], with two configurations—A (normal) and B (intruder). The fermion Hamiltonian, $\hat{H}_{\rm f}$, in Eq. (8) has the form

$$\hat{H}_{\rm f} = \begin{bmatrix} \sum_j \epsilon_j^{(\rm A)} \hat{n}_j & 0 \\ 0 & \sum_j \epsilon_j^{(\rm B)} \hat{n}_j \end{bmatrix}. \tag{9}$$

In Eq. (9), j is the angular momentum of the occupied orbit, $\hat{n}_j = \sum_\mu a^\dagger_{j\mu} a_{j\mu}$ is the number operator and $\epsilon_j^{(\rm i)}$ $(i = {\rm A}, {\rm B})$ are the single-particle energies for each configuration A or B. The boson-fermion interaction has the form

$$\hat{V}_{\rm bf} = \begin{bmatrix} \hat{V}_{\rm bf}^{\rm A}(\zeta^{(\rm A)}) & \hat{W}_{\rm bf}(\omega_j) \\ \hat{W}_{\rm bf}(\omega_j) & \hat{V}_{\rm bf}^{\rm B}(\zeta^{(\rm B)}) \end{bmatrix}. \tag{10}$$

In Eq. (10), $\hat{V}_{\rm bf}^{(i)}$ $(i = {\rm A}, {\rm B})$ is the boson-fermion interaction for each configuration, involving monopole, quadrupole, and exchange terms [54,55],

$$\hat{V}_{\rm bf}^{(i)} = V_{\rm bf}^{{\rm MON}(i)}\left(A_0^{(i)}\right) + V_{\rm bf}^{{\rm QUAD}(i)}\left(\Gamma_0^{(i)}\right) + V_{\rm bf}^{{\rm EXC}(i)}\left(\Lambda_0^{(i)}\right), \tag{11}$$

and $\hat{W}_{\rm bf}(\omega_j)$ is the Bose-Fermi mixing term. The explicit expressions are given in [55]. The microscopic interpretation of the IBFM [51] expresses Eq. (11) in terms of strengths $(A_0^{(i)}, \Gamma_0^{(i)}, \Lambda_0^{(i)})$ and occupation probabilities (u_j, v_j). For electromagnetic transitions of type σ and multipolarity L, the boson and fermion parts of the transitions operator read

$$\hat{T}(\sigma L) = \hat{T}_{\rm b}(\sigma L) + \hat{T}_{\rm f}(\sigma L). \tag{12}$$

The $\hat{T}_{\rm b}(E2)$ $[\hat{T}_{\rm b}(M1)]$ operator, for $E2$ $[M1]$ transition rates, is constructed of normal configuration A and intruder configuration B quadrupole (rotational) operators with effective charges $e^{(\rm A)}$ and $e^{(\rm B)}$ ($g^{(\rm A)}$, $g^{(\rm B)}$, $\tilde{g}^{(\rm A)}$, $\tilde{g}^{(\rm B)}$—see [55] for more details), respectively. The fermion part of the $\hat{T}(\sigma L)$ operator (12) is given by

$$\hat{T}_{\rm f}(\sigma L) = \sum_{jj'} f_{jj'}^{(L)} [a_j^\dagger \times \tilde{a}_{j'}]^{(L)} \tag{13}$$

with

$$f_{jj'}^{(L)} = \begin{cases} -\frac{e_f}{\sqrt{5}} \langle j || Y_{lm}^{(2)} || j' \rangle & \text{for } \sigma L = E2, \\ -\frac{f_1}{\sqrt{3}} \langle j || g_l \hat{l} + g_s \hat{s} || j' \rangle & \text{for } \sigma L = M1. \end{cases} \tag{14}$$

The e_f coefficient is the total effective charge and f_1 is the overall strength. For a proton, the free value for the angular g factor is $g_l = 1\,\mu_N$, and for the spin g factor we use a quenching of approximately 20%, i.e., $g_s = 4.42\,\mu_N$.

2. SCMF-IBFM

In the SCMF-IBFM framework we use the IBFM-2, which distinguishes between proton and neutron bosons. The corresponding Hamiltonian is given as [15]

$$\hat{H} = \hat{H}_B + \hat{H}_F^\nu + \hat{H}_{BF}^\nu. \tag{15}$$

In Eq. (15), $\hat{H}_B$ is the IBM-2 Hamiltonian, $\hat{H}_F^\nu$ is the single-neutron Hamiltonian, and $\hat{H}_{BF}^\nu$ is the Bose-Fermi interaction between the bosons and the neutron. For an even-even nucleus the IBM-2 Hamiltonian, providing a good description in the mass region of this work, is given by [15]

$$\hat{H}_B = \epsilon(\hat{n}_{d_\pi} + \hat{n}_{d_\nu}) + \kappa \hat{Q} \cdot \hat{Q} + \kappa' \sum_{\rho' \neq \rho} \hat{T}_{\rho\rho\rho'} + \kappa'' \hat{L} \cdot \hat{L} \tag{16}$$

with $\rho = \nu$ for neutrons and π for protons. In the first term on the right-hand side of Eq. (16), $\hat{n}_{d_\rho} = d_\rho^\dagger \cdot \tilde{d}_\rho$ corresponds to the d-boson number operator. The quadrupole operator, $\hat{Q}$, is defined as the sum of $\hat{Q}_\nu$ and $\hat{Q}_\pi$. $\hat{Q}_\rho$ is given by the expression $s_\rho^\dagger \tilde{d}_\rho + d_\rho^\dagger \tilde{s}_\rho + \chi_\rho [d_\rho^\dagger \times \tilde{d}_\rho]^{(2)}$. The third term involves a specific three-body boson interaction denoted as $\hat{T}_{\rho\rho\rho'}$. This interaction is represented as $\sum_L [d_\rho^\dagger \times d_\rho^\dagger \times d_{\rho'}^\dagger]^{(L)} \cdot [\tilde{d}_{\rho'} \times \tilde{d}_\rho \times \tilde{d}_\rho]^{(L)}$, where L denotes the total angular momentum of the boson system. It is worth mentioning that only the $L = 3$ terms are considered, as they play a crucial role in producing a minimum at $\gamma \approx 30°$, as observed in Refs. [57,58]. The last

term in Eq. (16) is the rotational term with the angular momentum operator $\hat{L} = \hat{L}_\nu + \hat{L}_\pi = \sqrt{10}\sum_{\rho=\nu,\pi}[d^\dagger_\rho \times \tilde{d}_\rho]^{(1)}$.

The second term of Eq. (15) is the single-neutron Hamiltonian [15]

$$\hat{H}^\nu_F = -\sum_{j_\nu} \epsilon_{j_\nu}\sqrt{2j_\nu+1}(\hat{a}^\dagger_{j_\nu} \times \tilde{\hat{a}}_{j_\nu})^{(0)} \tag{17}$$

with ϵ_{j_ν} being the single-particle energy of the spherical orbital j_ν whereas $\hat{a}^\dagger_{j_\nu}$ and $\hat{a}_{j_\nu}$ are the creation and annihilation operators, respectively. For the last term in Eq. (15), representing the interaction between the bosons and the neutron $\hat{H}^\nu_{BF}$, the commonly used form is employed [15]:

$$\hat{H}^\nu_{BF} = \Gamma_\nu \hat{Q}_{\nu'}\hat{q}_\nu + \Lambda_\nu \hat{V}_{\nu'\nu} + A_\nu \hat{n}_{d_\nu}\hat{n}_\nu \tag{18}$$

with $\nu' \neq \nu$ and Γ_ν, Λ_ν, and A_ν being strength parameters. It is assumed that the first two terms in Eq. (18), which describe the quadrupole and exchange interactions, are dominated by the interaction between unlike particles (i.e., between the odd proton and the neutron bosons or vice versa), whereas the third term, representing the monopole interactions, is dominated by the interaction of like particles (i.e., between the odd proton and the proton bosons).

The transition rates are readily computed using the eigenstates of the IBFM Hamiltonian, using fixed values for the boson effective charges $e^B_\pi = e^B_\nu = 0.10$ eb chosen so that the $B(E2; 2^+_1 \rightarrow 0^+_1)$ values for the deformed even-even core nuclei, i.e., ^{100,102}Zr, are reproduced [15]. The neutron effective charge $e^F = 0.5$ eb is adopted from earlier calculations [59]. In addition, the empirical g^B factors for the proton and neutron bosons, $g^B_\pi = 1.0\,\mu_N$ and $g^B_\nu = 0\,\mu_N$, respectively, are adopted and for the neutron g factors, the standard Schmidt values $g^\nu_l = 0\,\mu_N$ and $g^\nu_s = -3.82\,\mu_N$ are used [15]. Here, the structure of ^{99}Zr can be described as a system of an unpaired neutron coupled to the even-even boson-core ^{98}Zr. For the neutron valence space, the $3s_{1/2}$, $2d_{3/2}$, $2d_{5/2}$, and $1g_{7/2}$ spherical orbitals for positive-parity states are considered [15].

The values of the parameters ϵ, κ, χ_ν, χ_π, and κ' required to construct the IBM-2 Hamiltonian are determined by comparing the SCMF energy surface near the global minimum with the expectation value of the IBM-2 Hamiltonian in the boson coherent state [60]. In other words, we aim to make the IBM-2 energy surface ($E_{\rm IBM}$) approximately equal to that of the SCMF ($E_{\rm SCMF}$) by adjusting the IBM-2 parameters. The strength parameter κ'' of the $\hat{L}\cdot\hat{L}$ term is determined separately [61], by matching the cranking moment of inertia in the bosonic intrinsic state to the one computed by the SCMF within a specific range of β values ($|\beta| \leqslant 0.6$) [15]. This term generally makes a contribution to the moments of inertia of rotational bands [61]. The sign of the parameter κ' for the three-body boson term plays a certain role in determining the shape of the energy surface. In Ref. [15], κ' has been chosen to be positive for ^{94}Zr, so a triaxial minimum is obtained, while a negative sign of κ' has been obtained for all the other Zr nuclei resulting in two minima on the prolate and oblate sides. A previous calculation using the IBM framework has also utilized a three-body term to produce the two minima [62]. However, the impact of this term on the excitation spectra, except for the γ band [58], is relatively minor. Its contribution becomes even weaker when κ' has a negative sign. Consequently, the three-body boson terms are not considered in the present calculations for the odd-A Zr isotopes, which is also because the IBFM-2 code we have at hand only accommodates up to the two-body boson interactions. To determine the Hamiltonians for the single neutron ($\hat{H}^\nu_F$) and the boson-fermion interaction ($\hat{H}^\nu_{BF}$), a method of Ref. [53] is employed. The spherical single-particle energies (ϵ_j) and occupation probabilities (v^2_j) of the odd-neutron orbital j are obtained from the same constrained SCMF calculations, and these quantities are input to determine most of the parameters in $\hat{H}^\nu_F$ and $\hat{H}^\nu_{BF}$. The strength parameters (Γ_ν, Λ_ν, and A_ν) for the boson-fermion interaction are treated as adjustable parameters. These parameters are determined to reproduce the experimental low-lying positive-parity levels of ^{99}Zr. The criteria for fitting these parameters include achieving the correct spin for the ground state and reasonably accurate excitation energies of a few lowest yrast states. For a more detailed description, see Ref. [15].

B. Energy levels

1. ^{99}Nb

For the boson part of the Hamiltonian in Eq. (8) we take ^{98}Zr as the even-even core [56]. For the Bose-Fermi interaction in Eq. (11), the values of the strengths are $(A^{(i)}_0, \Gamma^{(i)}_0, \Lambda^{(i)}_0) = (-0.11, 1.0, 3.0)$ MeV (for both A and B configurations). The single-particle energies used in order to determine (u_j, v_j) and the single quasiparticle energies are taken from Table XI of [63] for the $1g_{9/2}$, $2p_{1/2}$, $2p_{3/2}$, $1f_{5/2}$ proton orbits. The $1g_{9/2}$ orbit is employ for a single-j calculation for the positive parity states, which the $2p_{1/2}$, $2p_{3/2}$, $1f_{5/2}$ orbits are employed for a multi-j calculation for the negative-parity states. The resulting positive- and negative-parity states are uncoupled. Therefore, the energies of the negative-parity states are shifted so that the lowest-lying known negative-parity state $E(1/2^-_1) = 365.3$ keV is reproduced [56].

Figure 5 shows the experimentally and theoretically determined low-lying energy levels. On the left side the positive parity states and on the right side the negative parity states are displayed.

For the positive-parity states of ^{99}Nb, the ground state is a result of the weak coupling between the 0^+_1 of the ^{98}Zr core, that belongs to configuration A, and the $\pi(1g_{9/2})$ orbit. The higher lying states, however, are all configuration B. The calculated $7/2^+_1$ originates from the coupling of the $\pi(1g_{9/2})$ with the 2^+_1 of ^{98}Zr. The calculated $9/2^+_2$ state, which is higher in energy, is mainly composed of the coupling between the $\pi(1g_{9/2})$ orbit and the 0^+_2 of ^{98}Zr. The different order in energy of the $7/2^+_1$ and $9/2^+_2$ state compared to lighter Nb isotopes is in accordance with the onset of deformation that has been identified in ^{98}Zr [16,56], before the ground states become of intruder character in the heavier isotopes with $A \geqslant 100$. Higher lying calculated states, such as the $5/2^+_1$ and $5/2^+_2$ correspond to the experimental $5/2^+_1$ and $5/2^+_2$, respectively. The calculated $3/2^+_1$ should correspond to the experimental $3/2^+_2$ since the latter has a measured strong $E2$ transition to the $5/2^+_1$ of > 45 W.u., where the calculation receives $3/2^+_1 \rightarrow 5/2^+_1 = 51$ W.u. [55]. The experimental $3/2^+_1$, $3/2^+_3$ do not have theoretical counterparts. The calcu-

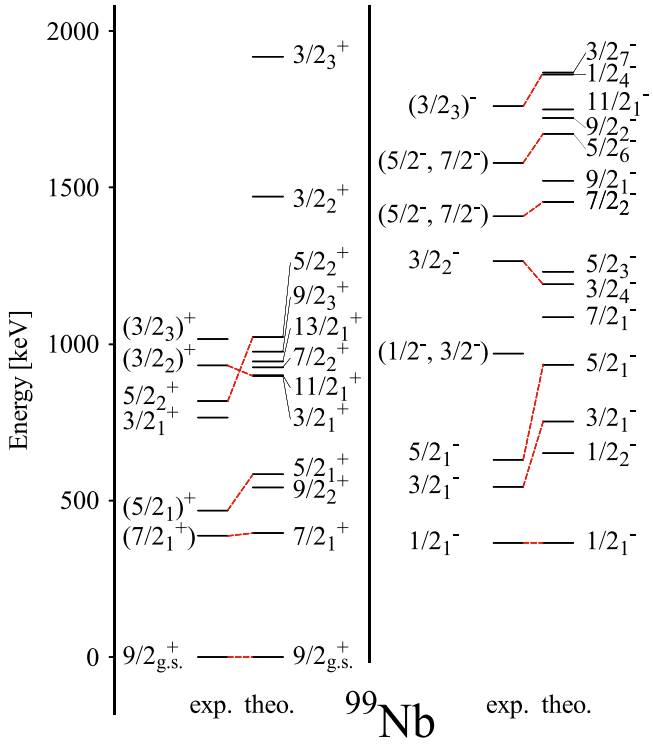

FIG. 5. Experimental [38] vs theoretical low energy level scheme of ^{99}Nb using IBFM-CM calculations. Positive (left) and negative parity (right) states are shown. Theoretically calculated states of the $K = 1/2_3^-$ band originating at 0.745 MeV are omitted for better clarity.

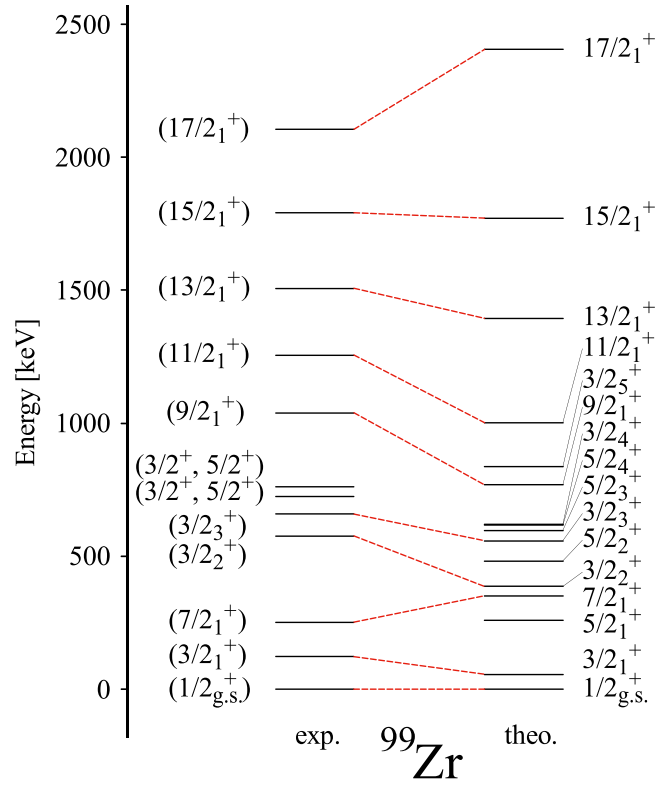

FIG. 6. Experimental [38] vs theoretical low energy level scheme of ^{99}Zr using SCMF-IBFM calculations. Here, only a selected choice of theoretical energy levels are displayed for better clarity.

lated $11/2_1^+, 7/2_2^+, 13/2_1^+, 9/2_3^+, 5/2_2^+$ states, not present in the experimental spectrum, originate from coupling different intruder states of the even-even core.

For the negative-parity state the $1/2_1^-$ is identified as the configuration A normal state that is generated from the coupling of the $\pi(2p_{1/2})$ orbit with the $0^+_{1;A}$ state of the adjacent ^{98}Zr isotope. Alongside it, there is a experimentally measured rotational band with $K^\pi = 3/2^-$ that is reproduced by the calculations to a reasonable degree. However, in contrast to experimentally determined values, the calculation suggests it to be a $K^\pi = 1/2^-$ band. Alongside this band, the calculation suggests another $K^\pi = 1/2^-$ band beginning at 0.745 MeV, which is not observed in the experimental data and is not shown in Fig. 5.

2. ^{99}Zr

In Fig. 6, the experimentally and theoretically determined low-lying energy levels of ^{99}Zr are shown. Only positive parity states, mainly of the yrast band [except for the $(3/2_2^+)$ and $(3/2_3^+)$ states measured in this work and two additional states, whose spins are not known yet], are displayed. Here, the theory is in a good agreement with the experimentally determined energies even for states with high excitation energies. As can already be seen in ^{99}Nb, the theoretical model generates states that have no observed experimental counterparts. Due to the highly selective character of β decay no uniform population of excited states in the daughter nucleus is expected.

The spins of two experimental states at 725 and 762 keV are still not known but are assumed to be either $3/2^+$ or $5/2^+$ states [48]. The theoretical model provides two $3/2^+$ and two $5/2^+$ states in this energy region, which makes the assignment more difficult. For example, the $5/2_1^+$ state at 260 keV predicted by the theoretical model might be the experimental state at 725 keV or the $3/2_5^+$ state at 835 keV could correspond to the state at 762 keV. This would lead to a change in the order of the states. However, since the order of the states with known spins does not change when comparing the experimental and theoretical models, the more reasonable agreement of states with unknown spins could correspond to the theoretically calculated $3/2^+$ and $5/2^+$ states at 597, 616, or 619 keV.

C. Transition probabilities

In the following section, experimentally determined transition probabilities are compared to theoretically calculated ones. Some decays can be of mixed $M1$ and $E2$ multipolarities, but without a known mixing ratio. For these cases the multipolarities in Tables II and III are marked with an asterisk. Further calculations with these transitions are assumed to be in the limit of pure $M1$ and $E2$ multipolarity and all possible combinations of $M1$ and $E2$ multipolarities for the decay branches are compared to the theoretical results.

TABLE II. ^{99}Nb: Comparison of the experimentally determined transition probabilities [$B_{\mathrm{exp}}(\sigma l)$] and the theoretically calculated reduced transition probabilities [$B_{\mathrm{theo}}(\sigma l)$]. The multipolarities with an asterisk are assumed in the pure $M1$ and $E2$ limits, respectively. For the $B(M1)$ values, approximately 1.8 μN^2 and for the $B(E2)$ values 27.2 $e^2\mathrm{fm}^4$ correspond to 1 W.u.

State	τ [ps]	Transition	E_γ [keV]	σl	$B_{\mathrm{exp}}(\sigma l)$	$B_{\mathrm{theo}}(\sigma l)$
$(7/2_1^+)$	22(3)	$(7/2_1^+) \rightarrow 9/2^+_{\mathrm{g.s.}}$	387.4(1)	$M1$	$0.044^{+7}_{-6}\ \mu N^2$	$0.011\ \mu N^2$
$(5/2_1)^+$	228(1)	$(5/2_1)^+ \rightarrow 9/2^+_{\mathrm{g.s.}}$	469.1(1)	$E2$	$146^{+2}_{-2}\ e^2\mathrm{fm}^4$	$27\ e^2\mathrm{fm}^4$
		$(5/2_1)^+ \rightarrow (7/2_1^+)$	81.8(1)	$M1^*$	$0.023^{+4}_{-4}\ \mu N^2$	$0.031\ \mu N^2$
		$(5/2_1)^+ \rightarrow 9/2^+_{\mathrm{g.s.}}$	469.1(1)	$E2$	$133^{+4}_{-4}\ e^2\mathrm{fm}^4$	$27\ e^2\mathrm{fm}^4$
		$(5/2_1)^+ \rightarrow (7/2_1^+)$	81.8(1)	$E2^*$	$4.5^{+7}_{-6} \times 10^4\ e^2\mathrm{fm}^4$	$0.133 \times 10^4\ e^2\mathrm{fm}^4$
$3/2_1^-$	113(2)	$3/2_1^- \rightarrow 1/2_1^-$	179.0(1)	$M1^*$	$0.081^{+2}_{-2}\ \mu N^2$	$0.004\ \mu N^2$
				$E2^*$	$3.35^{+9}_{-9} \times 10^4\ e^2\mathrm{fm}^4$	$0.0014 \times 10^4\ e^2\mathrm{fm}^4$

1. ^{99}Nb

In Table II the comparison of all possible combinations of experimentally and theoretically calculated transition probabilities of ^{99}Nb are shown. The $(7/2_1^+)$ state of ^{99}Nb has only one possible decay branch $[(7/2_1^+) \rightarrow 9/2^+_{\mathrm{g.s.}}(387.4\,\mathrm{keV})]$ with known $M1$ multipolarity, which can shed light on the nature of the mixing between the two configurations. The comparison of experimental and IBFM-CM values shows slight deviations, but they are of the same order of magnitude. This suggests the calculation is able to describe the mixing between the two configurations and the shape-coexistence phenomenon.

The $(5/2_1)^+$ state has two possible decay branches $[(5/2_1)^+ \rightarrow 9/2^+_{\mathrm{g.s.}}$ (469.1 keV) and $(5/2_1)^+ \rightarrow (7/2_1^+)$ (81.1 keV)], but only the $E2$ multipolarity of the 469.1 keV γ ray is known. The 81.8 keV γ ray is a mixed $M1/E2$ transition, though with yet unknown mixing ratio [38]. The obtained transition probabilities for the known 469.1 keV transition with an $E2$ multipolarity predicts a value close to 5 W.u., whereas the calculation gives 1 W.u., demonstrating

TABLE III. ^{99}Zr: Comparison of the experimentally determined reduced transition probabilities [$B_{\mathrm{exp}}(\sigma l)$] and the theoretically calculated reduced transition probabilities [$B_{\mathrm{theo}}(\sigma l)$]. The multipolarities with an asterisk are assumed in the pure $M1$ and $E2$ limit, respectively. For the $B(M1)$ values, approximately 1.8 μN^2 and for the $B(E2)$ values 27.2 $e^2\mathrm{fm}^4$ correspond to 1 W.u.

State	τ [ps]	Transition	E_γ [keV]	σl	$B_{\mathrm{exp}}(\sigma l)$	$B_{\mathrm{theo}}(\sigma l)$
$(3/2_1^+)$	1561(24)	$(3/2_1^+) \rightarrow (1/2^+_{\mathrm{g.s.}})$	121.7(1)	$M1$	$0.018^{+1}_{-1}\ \mu N^2$	$0.010\ \mu N^2$
$(7/2_1^+)$	$423(14) \cdot 10^3$	$(7/2_1^+) \rightarrow (3/2_1^+)$	130.2(1)	$E2$	$36^{+1}_{-1}\ e^2\mathrm{fm}^4$	$540\ e^2\mathrm{fm}^4$
$(3/2_2^+)$	437(18)	$(3/2_2^+) \rightarrow (1/2^+_{\mathrm{g.s.}})$	575.7(1)	$M1^*$	$0.00042^{+4}_{-4}\ \mu N^2$	$0.01911\ \mu N^2$
				$E2^*$	$18^{+2}_{-2}\ e^2\mathrm{fm}^4$	$28\ e^2\mathrm{fm}^4$
		$(3/2_2^+) \rightarrow (3/2_1^+)$	454.0(1)	$M1^*$	$0.00049^{+8}_{-7}\ \mu N^2$	$0.00774\ \mu N^2$
				$E2^*$	$34^{+6}_{-5}\ e^2\mathrm{fm}^4$	$5\ e^2\mathrm{fm}^4$
		$(3/2_2^+) \rightarrow (7/2_1^+)$	323.8(3)	$E2$	$13.3^{+28}_{-24}\ e^2\mathrm{fm}^4$	$0.2\ e^2\mathrm{fm}^4$
$(3/2_3^+)$	26(5)	$(3/2_3^+) \rightarrow (3/2_1^+)$	536.2(1)	$M1^*$	$0.012^{+3}_{-2}\ \mu N^2$	$0.002\ \mu N^2$
				$E2^*$	$579^{+147}_{-98}\ e^2\mathrm{fm}^4$	$267\ e^2\mathrm{fm}^4$
		$(3/2_3^+) \rightarrow (1/2^+_{\mathrm{g.s.}})$	658.0(4)	$M1^*$	$2.2^{+7}_{-5} \times 10^{-4}\ \mu N^2$	$39.4 \times 10^{-4}\ \mu N^2$
				$E2^*$	$7^{+2}_{-2}\ e^2\mathrm{fm}^4$	$258\ e^2\mathrm{fm}^4$
		$(3/2_3^+) \rightarrow (7/2_1^+)$	405.9(2)	$E2$	$421^{+129}_{-91}\ e^2\mathrm{fm}^4$	$14\ e^2\mathrm{fm}^4$
		$(3/2_3^+) \rightarrow (3/2_2^+)$	82.2(2)	$M1^*$	$0.10^{+5}_{-4}\ \mu N^2$	$0.01\ \mu N^2$
		$(3/2_3^+) \rightarrow (3/2_1^+)$	536.2(1)	$M1^*$	$0.011^{+3}_{-2}\ \mu N^2$	$0.002\ \mu N^2$
				$E2^*$	$552^{+141}_{-95}\ e^2\mathrm{fm}^4$	$267\ e^2\mathrm{fm}^4$
		$(3/2_3^+) \rightarrow (1/2^+_{\mathrm{g.s.}})$	658.0(4)	$M1^*$	$2.1^{+7}_{-5} \times 10^{-4}\ \mu N^2$	$39.4 \times 10^{-4}\ \mu N^2$
				$E2^*$	$7^{+2}_{-2}\ e^2\mathrm{fm}^4$	$258\ e^2\mathrm{fm}^4$
		$(3/2_3^+) \rightarrow (7/2_1^+)$	405.9(2)	$E2$	$441^{+136}_{-96}\ e^2\mathrm{fm}^4$	$14\ e^2\mathrm{fm}^4$
		$(3/2_3^+) \rightarrow (3/2_2^+)$	82.2(2)	$E2^*$	$2.1^{+9}_{-7} \times 10^5\ e^2\mathrm{fm}^4$	$0.0002\ e^2\mathrm{fm}^4$

the weak mixing between the configurations. Comparing both possible combinations with the theoretical model shows one large discrepancy. Assuming a pure $E2$ transition for the 81.8 keV γ ray, the theoretical calculations predict a transition probability of 49 W.u., while the experimentally determined transition probability is 1654 W.u. Thus, a more reasonable agreement can be obtained assuming a $M1$ type transition for the 81.8 keV γ ray. Here, experimental and theoretical values are close. Therefore, it might be assumed that the 81.8 keV transition is dominated by $M1$ multipolarity.

For the $3/2^-_1$ state, a comparison is quite complicated because both possible decay branches of this state [$3/2^-_1 \rightarrow 1/2^-_1$ (179.0 keV) and $3/2^-_1 \rightarrow (5/2_1)^+$ (74.3 keV)] have unknown multipolarities, resulting in four possible combinations. The 179.0 keV γ ray is either a $M1$ or $E2$ transition, while the 74.3 keV γ ray has $E1$ or $M2$ multipolarity. Since no numerical framework exists to calculate $E1$ or $M2$ transitions within the framework of the IBFM-CM [64], no assumptions about the 74.3 keV transition are possible. Furthermore, the influence of the multipolarity of the 74.3 keV transition on the $B(M1)$ and $B(E2)$ values for the 179.0 keV transition is only about 1% and thus not shown in Table II. Nevertheless, assumptions can be made about the 179.0 keV transition. Having a relative intensity of 100 in contrast to the 0.2 of the 74.3 keV γ ray, this transition completely dominates the de-excitation of the $3/2^-_1$ state. Comparing only the experimental and theoretical values for the 179.0 keV transition, the most consistent results are obtained for the $M1$ multipolarity. Therefore, it could be assumed that an $M1$ multipolarity is favored in this case.

2. ^{99}Zr

In Table III the comparison between experimentally and theoretically calculated transition probabilities of ^{99}Zr are shown. The $(3/2^+_1)$ state of ^{99}Zr has only one possible decay branch [$(3/2^+_1) \rightarrow (1/2^+_{g.s.})$ (121.7 keV)] with known $M1$ multipolarity. The comparison of experimental and IBFM values shows slight deviations, but they are in the same order of magnitude.

The $(7/2^+_1)$ state was not measured in this work, but since its lifetime is well known [65], it is also compared to theoretical calculations. It also has one possible decay branch [$(7/2^+_1) \rightarrow (3/2^+_1$ (130.2 keV)] but with known $E2$ multipolarity. Here, the theoretically calculated value of 20 W.u. predicts collective behavior whereas the experimentally calculated value of 1.3 W.u. does not.

The $(3/2^+_2)$ state has three possible decay branches [$(3/2^+_2) \rightarrow (1/2^+_{g.s.})$ (575.7 keV), $(3/2^+_2) \rightarrow (3/2^+_1)$ (454.0 keV) and $(3/2^+_2) \rightarrow (7/2^+_1)$ (323.8 keV)]. The 575.7 and 454.0 keV γ rays are either $M1$ or $E2$ transitions, whereas the multipolarity of the 323.8 keV γ ray is a $E2$ ($M3$, $E4$,...) transition. Since $M3$, $E4$,... transitions are very unlikely compared to an $E2$ transition, the pure $E2$ limit of the 323.8 keV γ ray is assumed for all combinations. Comparing all four possible combinations with the theoretical model shows large discrepancies. Transition probabilities for an assumed $E2$ transition for the 454.0 keV γ ray predict a hint of collectivity, whereas the theoretical model predict a less collective behavior. Best agreement is achieved when the 575.7 and 454.0 keV γ rays are assumed as $E2$ multipolarity, but theoretically calculated reduced transition probabilities differs around one order of magnitude for these transitions, which might indicate a mixed $M1/E2$ character. The assumed 323.8 keV $E2$ transition can not be reproduced in all of the four possible combinations.

It is even more complicated to compare the results of the $(3/2^+_3)$ state, since this state has four decay branches [$(3/2^+_3) \rightarrow (3/2^+_1)$ (536.2 keV), $(3/2^+_3) \rightarrow (1/2^+_{g.s.})$ (658.0 keV), $(3/2^+_3) \rightarrow (7/2^+_1)$ (405.9 keV) and $(3/2^+_3) \rightarrow (3/2^+_2)$ (82.2 keV)]. Here, the 405.9 keV γ ray is a $E2$ ($M3$, $E4$,...) transition, again assuming a pure $E2$ limit for all possible combinations. All other transitions have either $M1$ or $E2$ multipolarities, which results in eight possible combinations. Assuming $E2$ multipolarity for 536.2, 658.0 and 82.2 keV transitions, the resulting transition probabilities predict strong collective behavior, which is partially confirmed by the theoretical model. Best agreement with the theoretical predictions is achieved for an assumed $M1$ multipolarity for the 658.0 and 82.2 keV γ rays and an $E2$ multipolarity for the 536.2 keV γ ray. Here, the 536.2 keV γ ray shows a good agreement in the same order of magnitude, whereas the 658.0 and 82.2 keV γ rays differs one order of magnitude. The assumed 405.9 keV $E2$ transition fits worst. It should be noted, that the used model does not fit its parameters to experimental data, but rather to potential energy surfaces that are the result of constrained relativistic Hartree-Bogoliubov calculations. Nevertheless, the theory does not bring the desired results, since most of the theoretically calculated values are so small. This might be due to the fact that shape-coexisting, as assumed for this nucleus [49], is absent in the model. Just for an assumed $E2$ multipolarity of the 536.2 and 658.0 keV γ rays of the $(3/2^+_3)$ state, the theoretically calculated values predict collectivity, where only the 536.2 keV γ ray fits with the experimentally determined values.

VI. CONCLUSIONS

In this work, the analysis of an experiment at the LOHENGRIN spectrometer at the Institut Laue-Langevin was performed to investigate lifetimes of low-lying states in ^{99}Zr and ^{99}Nb. In ^{99}Zr the states $(3/2^+_1)$, $(3/2^+_2)$, and $(3/2^+_3)$ were measured. Here, the lifetimes of all states are in good agreement with the literature values [47–49], while the uncertainties could be significantly decreased. In ^{99}Nb the states $(7/2^+_1)$, $(5/2_1)^+$, $3/2^-_1$, and $(1/2^+, 3/2^+)$ were measured, while the actual spin of the state $(1/2^+, 3/2^+)$ is not known yet. Compared with literature values, the determined lifetimes of states $(7/2^+_1)$ and $(1/2^+, 3/2^+)$ are in good agreement [43,44]. The other states differs significantly [43–45,47]. Since most of the literature values are measured in the last century, the determined lifetimes in this work seems more reliable due to an improvement of the fast-timing technique in the last years.

Reduced transition probabilities, calculated via the experimentally determined lifetimes, were compared to two different IBFM calculations. Since most of the transitions have unknown multipolarity, comparison between experi-

TABLE IV. All necessary data used to determine the final lifetimes of ^{99}Nb and ^{99}Zr that have not yet been shown. Values for the gates and peak-to-background ratios also needed for final calculations as well as the final lifetimes can be found in Table I.

Nucleus	State	PRD	$\Delta C_{\text{Compton}}$ [ps]	ΔC_{exp} [ps]
^{99}Nb	$(7/2_1^+)$	108(5)	−179(12)	107(3)
		−9(2)	−345(5)	
	$(5/2_1)^+$	−25(1)	401(2)	443(2)
		−19(1)	47(3)	
	$3/2_1^-$	−13(2)	364(3)	188(2)
		41(3)	259(5)	
	$(1/2^+, 3/2^+)$	149(4)	44(3)	151(5)
		−27(1)	−31(8)	
^{99}Zr	$(3/2_1^+)$	−28(1)	–	–
		72(5)		
	$(3/2_2^+)$	11(2)	−28(7)	366(7)
		−26(1)	−162(1)	
	$(3/2_3^+)$	36(3)	−61(4)	67(9)
		−24(1)	−179(8)	

mental and theoretical calculations is not yet conclusive. Furthermore, some of the transitions are assumed to be of mixed multipolarity but without a given mixing ratio. All of these unknown properties add complexity due to multiple possible combinations of transitions. Therefore, a clear comparison is almost impossible, especially for ^{99}Zr. Some of the calculated transition probabilities of both nuclei predict collective behavior as well as single particle transitions in almost all possible combinations. The shape-coexistence phenomenon, which is proposed in several previous works in this mass region [49,66], is investigated by the IBFM approaches for the positive- and negative-parity states. The IBFM-CM, describes the positive- and some of the negative-parity energies, and is able to describe the measured mixing between the positive-parity configurations. The SCMF-IBFM, describes the higher lying yrast band states and some of their transitions.

Comparing experimental and theoretical energy level schemes of ^{99}Zr shows good agreement for known experimental states up to 2 MeV. Experimental states with unknown spins cannot be clearly attributed to a theoretically calculated spin, since several possible theoretical states with almost the same energy occur in this energy range and thus different solutions would be possible. For ^{99}Nb, the low energy of the positive- and negative-parity states are in good agreement to the theoretical model, where some of the experimental levels do not have calculated counterparts. For both ^{99}Zr and ^{99}Nb there are additional theoretically calculated states that have no observed experimental counterparts yet.

The intricate relationship between the single-particle degrees of freedom and collective behavior challenges the current theoretical models and adds insight, also over the adjacent even-even isotopes. It suggests further investigations should be undertaken in this region and nuclei, also experimentally, in order to comprehend better the occurrence of shape-coexistence and configuration mixing. It would thus be insightful to try and find the proposed calculated $9/2_2^+$ at 542 keV of ^{99}Nb, belonging to the intruder configurations, and assign the spins for the 725 and 762 keV levels for ^{99}Zr and look for the other predicted states in this energy region.

One possibility for future measurements is to aim for the assignments for the unknown multipolarities of transitions. By accurately determining the multipolarities associated with certain transitions, the comparison between experimental and theoretically calculated states would be more effective. Another possible direction is to look for additional transitions that come from other $3/2^-$ states in ^{99}Nb or from the $7/2_1^+$ state in ^{99}Zr. These transitions can provide valuable data on the energy levels and quantum properties of the nucleus. By identifying and studying such transitions, we can expand our knowledge of the nuclear structure and potentially discover new patterns or phenomena that were previously unexplored.

ACKNOWLEDGMENTS

This work was supported by the Deutsche Forschungsgemeinschaft (DFG) under Grant No. JO 391/18-1. We also want to thank the team of the nuclear reactor for the operation at the ILL.

APPENDIX: ALL DATA USED TO DETERMINE THE LIFETIMES

All necessary data used to determine the lifetimes in this work for the nuclei ^{99}Nb and ^{99}Zr that have not yet been shown are listed in Table IV.

[1] P. Cejnar, J. Jolie, and R. F. Casten, Rev. Mod. Phys. **82**, 2155 (2010).
[2] K. Heyde and J. L. Wood, Rev. Mod. Phys. **83**, 1467 (2011).
[3] H. L. Thayer, J. Billowes, P. Campbell, P. Dendooven, K. T. Flanagan, D. H. Forest, J. A. R. Griffith, J. Huikari, A. Jokinen, R. Moore, A. Nieminen, G. Tungate, S. Zemlyanoi, and J. Äystö, J. Phys. G: Nucl. Part. Phys. **29**, 2247 (2003).
[4] E. Cheifetz, R. Jared, S. Thompson, and J. Wilhelmy, Phys. Rev. Lett. **25**, 38 (1970).
[5] B. Pritychenko, M. Birch, B. Singh, and M. Horoi, At. Data Nucl. Data Tables **107**, 1 (2016).
[6] I. Angeli and K. P. Marinova, At. Data Nucl. Data Tables **99**, 69 (2013).
[7] R. K. Sheline, I. Ragnarsson, and S. Nilsson, Phys. Lett. B **41**, 115 (1972).
[8] A. Kumar and M. R. Gunye, Phys. Rev. C **32**, 2116 (1985).
[9] R. Rodríguez-Guzmán, P. Sarriguren, L. M. Robledo, and S. Perez-Martin, Phys. Lett. B **691**, 202 (2010).

[10] F. Flavigny, P. Doornenbal, A. Obertelli, J.-P. Delaroche, M. Girod, J. Libert, T. R. Rodriguez, G. Authelet, H. Baba, D. Calvet, F. Château, S. Chen, A. Corsi, A. Delbart, J.-M. Gheller, A. Giganon, A. Gillibert, V. Lapoux, T. Motobayashi, M. Niikura *et al.*, Phys. Rev. Lett. **118**, 242501 (2017).

[11] D. A. Sazonov, E. A. Kolganova, T. M. Shneidman, R. V. Jolos, N. Pietralla, and W. Witt, Phys. Rev. C **99**, 031304(R) (2019).

[12] V. Karayonchev, J. Jolie, A. Blazhev, A. Dewald, A. Esmaylzadeh, C. Fransen, G. Häfner, L. Knafla, J. Litzinger, C. Müller-Gatermann, J.-M. Régis, K. Schomacker, A. Vogt, N. Warr, A. Leviatan, and N. Gavrielov, Phys. Rev. C **102**, 064314 (2020).

[13] S. Ansari, J.-M. Régis, J. Jolie, N. Saed-Samii, N. Warr, W. Korten, M. Zielińska, M.-D. Salsac, A. Blanc, M. Jentschel, U. Köster, P. Mutti, T. Soldner, G. S. Simpson, F. Drouet, A. Vancraeyenest, G. de France, E. Clément, O. Stezowski, C. A. Ur *et al.*, Phys. Rev. C **96**, 054323 (2017).

[14] W. Urban, T. Rzaca-Urban, J. Wiśniewski, A. G. Smith, G. S. Simpson, and I. Ahmad, Phys. Rev. C **100**, 014319 (2019).

[15] K. Nomura, T. Nikšić, and D. Vretenar, Phys. Rev. C **102**, 034315 (2020).

[16] N. Gavrielov, A. Leviatan, and F. Iachello, Phys. Rev. C **99**, 064324 (2019).

[17] M. Büscher, R. F. Casten, R. L. Gill, R. Schuhmann, J. A. Winger, H. Mach, M. Moszyński, and K. Sistemich, Phys. Rev. C **41**, 1115 (1990).

[18] E. Clément, M. Zielińska, A. Görgen, W. Korten, S. Péru, J. Libert, H. Goutte, S. Hilaire, B. Bastin, C. Bauer, A. Blazhev, N. Bree, B. Bruyneel, P. A. Butler, J. Butterworth, P. Delahaye, A. Dijon, D. T. Doherty, A. Ekström, C. Fitzpatrick *et al.*, Phys. Rev. Lett. **116**, 022701 (2016).

[19] H. Mach, F. K. Wohn, M. Moszynski, R. L. Gill, and R. F. Casten, Phys. Rev. C **41**, 1141 (1990).

[20] Å. W. Iskra, B. Fornal, S. Leoni, G. Bocchi, A. Petrovici, C. Porzio, A. Blanc, G. D. France, M. Jentschel, U. Köster, P. Mutti, J.-M. Régis, G. Simpson, T. Soldner, C. A. Ur, W. Urban, D. Bazzacco, G. Benzoni, S. Bottoni, A. Bruce *et al.*, Europhys. Lett. **117**, 12001 (2017).

[21] B. Cheal, M. Gardner, M. Avgoulea, J. Billowes, M. Bissell, P. Campbell, T. Eronen, K. Flanagan, D. Forest, J. Huikari, A. Jokinen, B. Marsh, I. Moore, A. Nieminen, H. Penttilä, S. Rinta-Antila, B. Tordoff, G. Tungate, and J. Äystö, Phys. Lett. B **645**, 133 (2007).

[22] G. Lhersonneau, B. Pfeiffer, K.-L. Kratz, T. Enqvist, P. P. Jauho, A. Jokinen, J. Kantele, M. Leino, J. M. Parmonen, H. Penttilä, and J. Äystö, Phys. Rev. C **49**, 1379 (1994).

[23] W. Witt, V. Werner, N. Pietralla, M. Albers, A. D. Ayangeakaa, B. Bucher, M. P. Carpenter, D. Cline, H. M. David, A. Hayes, C. Hoffman, R. V. F. Janssens, B. P. Kay, F. G. Kondev, W. Korten, T. Lauritsen, O. Möller, G. Rainovski, G. Savard, D. Seweryniak *et al.*, Phys. Rev. C **98**, 041302(R) (2018).

[24] W. Urban, J. Durell, A. Smith, W. Phillips, M. Jones, B. Varley, T. Rząca-Urban, I. Ahmad, L. Morss, M. Bentaleb, and N. Schulz, Nucl. Phys. A **689**, 605 (2001).

[25] W. Urban, J. A. Pinston, T. Rzaca-Urban, A. Złomaniec, G. Simpson, J. L. Durell, W. R. Phillips, A. G. Smith, B. J. Varley, I. Ahmad, L. R. Morss, M. Bentaleb, and N. Schulz, Eur. Phys. J. A **16**, 11 (2003).

[26] C. Kremer, S. Aslanidou, S. Bassauer, M. Hilcker, A. Krugmann, P. von Neumann-Cosel, T. Otsuka, N. Pietralla, V. Y. Ponomarev, N. Shimizu, M. Singer, G. Steinhilber, T. Togashi, Y. Tsunoda, V. Werner, and M. Zweidinger, Phys. Rev. Lett. **117**, 172503 (2016).

[27] P. Federman and S. Pittel, Phys. Rev. C **20**, 820 (1979).

[28] U. Köster, H. Faust, T. Materna, and L. Mathieu, Nucl. Instrum. Methods Phys. Res. A **613**, 363 (2010).

[29] P. Armbruster, M. Asghar, J. Bocquet, R. Decker, H. Ewald, J. Greif, E. Moll, B. Pfeiffer, H. Schrader, F. Schussler, G. Siegert, and H. Wollnik, Nucl. Instrum. Methods **139**, 213 (1976).

[30] G. Fioni, H. Faust, M. Gross, M. Hesse, P. Armbruster, F. Gönnenwein, and G. Münzenberg, Nucl. Instrum. Methods Phys. Res. A **332**, 175 (1993).

[31] A. Esmaylzadeh, J.-M. Régis, Y. H. Kim, U. Köster, J. Jolie, V. Karayonchev, L. Knafla, K. Nomura, L. M. Robledo, and R. Rodríguez-Guzmán, Phys. Rev. C **100**, 064309 (2019).

[32] J.-M. Régis, A. Esmaylzadeh, J. Jolie, V. Karayonchev, L. Knafla, U. Köster, Y. Kim, and E. Strub, Nucl. Instrum. Methods Phys. Res. A **955**, 163258 (2020).

[33] A. Esmaylzadeh *et al.*, https://dx.doi.org/10.5291/ILL-DATA.3-01-689.

[34] J.-M. Régis, N. Saed-Samii, M. Rudigier, S. Ansari, M. Dannhoff, A. Esmaylzadeh, C. Fransen, R.-B. Gerst, J. Jolie, V. Karayonchev, C. Müller-Gatermann, and S. Stegemann, Nucl. Instrum. Methods Phys. Res. A **823**, 72 (2016).

[35] J.-M. Régis, M. Dannhoff, and J. Jolie, Nucl. Instrum. Methods Phys. Res. A **897**, 38 (2018).

[36] J.-M. Régis, G. Pascovici, J. Jolie, and M. Rudigier, Nucl. Instrum. Methods Phys. Res. A **622**, 83 (2010).

[37] J.-M. Régis, G. Simpson, A. Blanc, G. de France, M. Jentschel, U. Köster, P. Mutti, V. Paziy, N. Saed-Samii, T. Soldner, C. Ur, W. Urban, A. Bruce, F. Drouet, L. Fraile, S. Ilieva, J. Jolie, W. Korten, T. Kröll, S. Lalkovski *et al.*, Nucl. Instrum. Methods Phys. Res. A **763**, 210 (2014).

[38] E. Browne and J. K. Tuli, Nucl. Data Sheets **112**, 275 (2011).

[39] L. Knafla, A. Harter, M. Ley, A. Esmaylzadeh, J.-M. Régis, D. Bittner, A. Blazhev, F. von Spee, and J. Jolie, Nucl. Instrum. Methods Phys. Res. A **1052**, 168279 (2023).

[40] Z. Bay, Phys. Rev. **77**, 419 (1950).

[41] J.-M. Régis, H. Mach, G. Simpson, J. Jolie, G. Pascovici, N. Saed-Samii, N. Warr, A. Bruce, J. Degenkolb, L. Fraile, C. Fransen, D. Ghita, S. Kisyov, U. Koester, A. Korgul, S. Lalkovski, N. Mărginean, P. Mutti, B. Olaizola, Z. Podolyak *et al.*, Nucl. Instrum. Methods Phys. Res. A **726**, 191 (2013).

[42] V. Karayonchev, A. Blazhev, A. Esmaylzadeh, J. Jolie, M. Dannhoff, F. Diel, F. Dunkel, C. Fransen, L. M. Gerhard, R.-B. Gerst, L. Knafla, L. Kornwebel, C. Müller-Gatermann, J.-M. Régis, N. Warr, K. O. Zell, M. Stoyanova, and P. Van Isacker, Phys. Rev. C **99**, 024326 (2019).

[43] H. Ohm *et al.*, Jul-Spez-562, 34 (1990).

[44] M. Rudigier, Ph.D. thesis, Universität zu Köln, Institut für Kernphysik, 2013, https://kups.ub.uni-koeln.de/5584/.

[45] G. Lhersonneau, B. Pfeiffer, J. R. Persson, J. Suhonen, J. Toivanen, P. Campbell, P. Dendooven, A. Honkanen, M. Huhta, P. M. Jones, R. Julin, S. Juutinen, M. Oinonen, H. Penttilä, K. Peräjärvi, A. Savelius, W. Jicheng, J. C. Wang, and J. Äystö, Z. Phys. A **358**, 317 (1997).

[46] G. Battistuzzi, K. Kawade, H. Lawin, K. Shizuma, and K. Sistemich, Z. Phys. A **306**, 113 (1982).

[47] G. Lhersonneau, H. Gabelmann, N. Kaffrell, K. L. Kratz, and B. Pfeiffer, Z. Phys. A **332**, 243 (1989).

[48] G. Lhersonneau and S. Brant, Phys. Rev. C **72**, 034308 (2005).

[49] P. Spagnoletti, G. Simpson, S. Kisyov, D. Bucurescu, J.-M. Régis, N. Saed-Samii, A. Blanc, M. Jentschel, U. Köster, P. Mutti, T. Soldner, G. de France, C. A. Ur, W. Urban, A. M. Bruce, C. Bernards, F. Drouet, L. M. Fraile, L. P. Gaffney, D. G. Ghiță *et al.*, Phys. Rev. C **100**, 014311 (2019).
[50] B. Olsen and L. Boström, Nucl. Instrum. Methods **44**, 65 (1966).
[51] F. Iachello and P. Van Isacker, *The Interacting Boson-Fermion Model* (Cambridge University Press, Cambridge, 1991).
[52] F. Iachello and O. Scholten, Phys. Rev. Lett. **43**, 679 (1979).
[53] K. Nomura, T. Nikšić, and D. Vretenar, Phys. Rev. C **93**, 054305 (2016).
[54] N. Gavrielov, A. Leviatan, and F. Iachello, Phys. Rev. C **106**, L051304 (2022).
[55] N. Gavrielov, Phys. Rev. C **108**, 014320 (2023).
[56] N. Gavrielov, A. Leviatan, and F. Iachello, Phys. Rev. C **105**, 014305 (2022).
[57] K. Nomura, R. Rodríguez-Guzmán, and L. M. Robledo, Phys. Rev. C **94**, 044314 (2016).
[58] K. Nomura, N. Shimizu, D. Vretenar, T. Nikšić, and T. Otsuka, Phys. Rev. Lett. **108**, 132501 (2012).
[59] K. Nomura, R. Rodríguez-Guzmán, and L. M. Robledo, Phys. Rev. C **101**, 014306 (2020).
[60] K. Nomura, N. Shimizu, and T. Otsuka, Phys. Rev. Lett. **101**, 142501 (2008).
[61] K. Nomura, T. Otsuka, N. Shimizu, and L. Guo, Phys. Rev. C **83**, 041302(R) (2011).
[62] A. Leviatan and D. Shapira, Phys. Rev. C **93**, 051302(R) (2016).
[63] J. Barea and F. Iachello, Phys. Rev. C **79**, 044301 (2009).
[64] N. Gavrielov (private communication) (2022).
[65] H. Selič, G. Sadler, T. Khan, W. D. Lauppe, H. Lawin, K. Sistemich, E. Monnand, J. Blachot, J. Bocquet, and F. Schussler, Z. Phys. A **289**, 197 (1979).
[66] E. T. Gregor, M. Scheck, R. Chapman, L. P. Gaffney, J. Keatings, K. R. Mashtakov, D. O'Donnell, J. F. Smith, P. Spagnoletti, M. Thürauf, V. Werner, and C. Wiseman, Eur. Phys. J. A **53**, 50 (2017).